Load-Dependent Critical Temperatures for Standard Fire Resistance of W-Shape Floor Beam Assemblies: Experimental Validation and Simplified Analysis

MICHAEL M. DRURY and SPENCER E. QUIEL

ABSTRACT

Comprehensive results of ASTM E119 (2019) standard fire tests (performed by AISC/AISI in 2015) are used to validate load-dependent critical temperature relationships that conservatively predict the thermally induced loss of flexural resistance for W-shape floor beam assemblies. The 16 tested assemblies used the same W8×28 section (coated with the same thickness of passive spray-applied fire resistive material), supported 2½ in. (64 mm) of lightweight concrete (reinforced with welded wire mesh) on a 2 in. (51 mm) corrugated metal deck, and had a clear span of 154¾ in. (3.93 m) in one-way bending. Four specimen groups in the following configurations were tested with four specimens each: restrained ends with composite slab, unrestrained ends with composite slab, restrained ends with noncomposite slab, and unrestrained ends with noncomposite slab. The four specimens in each group were each tested with a constant applied flexural load but at a range of magnitudes, inducing maximum bending moment from 23 to 60% of the section's ambient nominal moment capacity. The results of these tests clearly demonstrate a relationship between the loss of flexural resistance and the increase in steel beam temperature (particularly the bottom flange temperature) as a function of applied loading. The fire-induced temperature increases in the protected steel beams are then used to validate lumped mass thermal calculations per the AISC *Specification* (2022) and Part 1-2 of Eurocodes 3 and 4 (CEN, 2005, 2008), which are classified as simple analysis methods per Section A-4.2.4d of the AISC *Specification.* The results of this study demonstrate that simplified thermal analysis methods can be combined with load-dependent critical temperature relationships to conservatively predict the standard fire resistance of W-shape floor beam assemblies at the onset of flexural failure.

Keywords: standard fire resistance design (SFRD), W-shape steel floor beam assembly, composite vs. noncomposite slab, restraint of thermal expansion, critical steel temperature at flexural runaway, hourly fire resistance ratings.

INTRODUCTION

Floor systems in North American steel-framed building construction are often comprised of wide-flange (i.e., W-shape) beams that support a concrete slab. Beams that are not part of a moment-resisting frame are typically designed as one-way simple spans that are supported by shear connections. The slab is typically reinforced with steel bars or welded wire reinforcement (WWR) and is cast onto corrugated or fluted light-gage metal decking. The beam and slab are often constructed to be composite at their interface, thus achieving a degree of strain compatibility and amplifying their collective flexural stiffness and moment capacity. Composite action is commonly developed by welding headed shear studs at regularly spaced intervals through the metal deck to the top flange of the beam prior to concrete placement (see Figure 1).

Floor beams often require the application of passive fire protection to meet minimum hourly fire resistance ratings as a function of the building's size, occupancy, and purpose per the International Building Code (IBC) (ICC, 2020). Passive fire protection for W-shape beams in current practice often consists of spray-applied fire-resistive material (SFRM), which is a lightweight cementitious product with high thermal resistance. Due to their sheer quantity, floor beams can require a significant portion of the overall amount of SFRM applied to all steel framing throughout the building. Hourly fire resistance ratings describe the time needed to exceed a thermal or structural limit criterion when the assembly is subjected to a "standard fire" heating regime, such as those provided in ASTM E119 (2019), UL 263 (2020), or ISO 834 (2019). As shown in Figure 2, these temperature time histories undergo a rapid rise during the first 10 min, after which the rate of temperature increase slows before approaching 2000°F (1093°C) after 3 hr. Beyond that time, these high temperatures would continue to gradually increase with no subsequent decay phase or any consideration of suppression from sprinklers (i.e., active fire protection). The initial 2 hr period of a standard fire curve is intended to generally represent the ramp-up of temperature in a post-flashover building compartment, and

Michael M. Drury, Associate, Wiss, Janney, Elstner Associates, Inc., Princeton, N.J. Email: mdrury@wje.com

Spencer E. Quiel, Associate Professor, Department of Civil and Environmental Engineering, Lehigh University, Bethlehem, Pa. Email: seq213@lehigh.edu (corresponding)

the indefinite continuation of high temperature exposure will ensure that the thermal and/or structural performance criteria limits are eventually reached.

For comparison, a "natural" fire temperature time history would increase as a function of the geometry, fuel load, ventilation, and material characteristics of a given building compartment (CEN, 2009) and then eventually enter a subsequent decay phase until burnout. A representative natural fire curve from a previous study by the authors (Drury and Quiel, 2023a) is plotted for comparison in Figure 2. A natural fire curve can be used to evaluate the survivability and resilience of a structural assembly to a realistic fire exposure. Such considerations are outside the scope of this

paper, but the reader is referred to several recent publications by ASCE for more guidance (ASCE, 2020; LaMalva, 2018).

In a typical standard fire evaluation, a floor beam assembly (which includes a supported slab) with an SFRM-protected W-shape section is heated from below while carrying a flexural load. Standard fire tests for floor beam assemblies are conducted as either restrained (i.e., the ends of the beam are fully restricted from axial thermal expansion or rotation) or unrestrained (i.e., the beam ends are free to thermally expand and rotate). These idealized configurations do not represent actual boundary conditions in a building but are intended to bracket the partial restraint
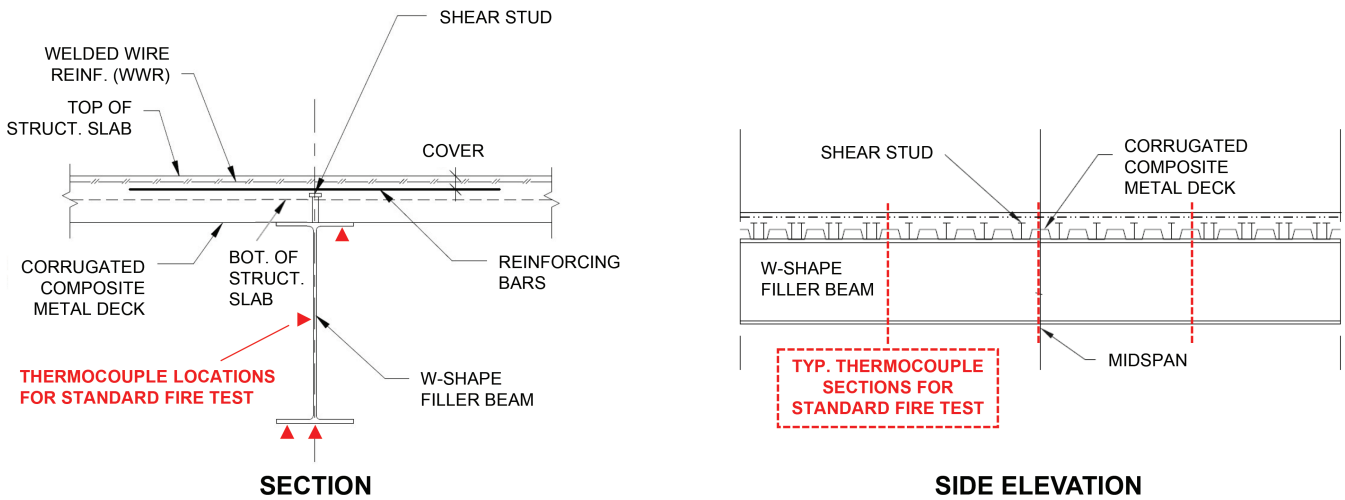

Fig. 1. Representative illustration of a composite W-shape floor beam, including thermocouple placement for an ASTM E119 standard fire test.
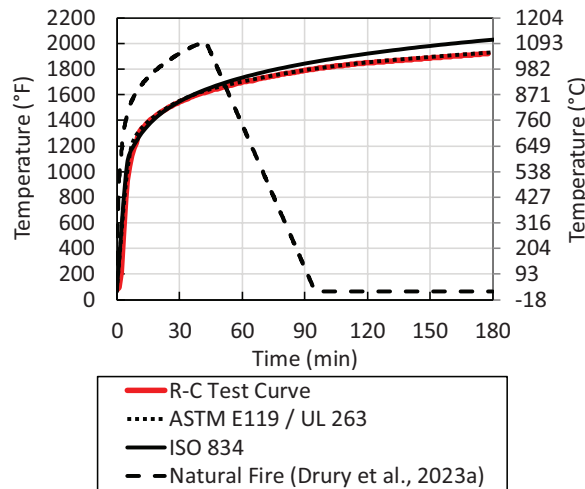

Fig. 2. Comparison of the R-C test's furnace temperature time history with select standard and natural fire curves.

Table 1. Temperature and Deflection Performance Limits per Published Standards for Standard Fire Testing of W-Shape Floor Beam Assemblies		
Type of Limit	**Source**	**Limit**
Midspan deflection	ASTM E119-19	• Midspan deflection: $L^2/(400d)$ THEN • Deflection rate per minute: $L^2/(9000d)$
	BS 476-21:1987	• Midspan deflection: $L/20$
Critical temperature of steel beam	ASTM E119-19	• Average steel beam temperature from 4 thermocouples per Figure 1 ($T_{s,E119}$): 1100°F (593°C) AND • Maximum steel beam temperature at a single thermocouple ($T_{s,MAX}$): 1300°F (704°C)
Critical temperature transmission through slab	ASTM E119-19	• Average temperature increase above ambient at the unexposed top-of-slab surface: 250°F (139°C) AND • Maximum temperature increase above ambient at any point on the unexposed top-of-slab surface: 325°F (181°C)

to thermal expansion and end rotation that would be provided by realistic connections and a continuous reinforced concrete floor slab. The heated assembly is monitored for its ability to sustain the applied flexural load as well as for the temperature increase in the steel beam and thermal transmission through the concrete slab. The time at which a given criteria is met is then rounded down to the nearest half-hour to denote the hourly fire resistance rating for the tested section configuration. Standard fire resistance design (SFRD), which is widely used in current practice, uses these hourly ratings as a comparative indicator of ultimate capacity under a standardized fire exposure.

Table 1 summarizes the thermal and structural performance limit criteria that are used to signify "failure" during a standard fire test of a composite steel floor beam. The deflection limits per ASTM E119 (2019) or BS 476 (BSI, 2008, 1987) are intended to represent a loss of flexural resistance (i.e., at or near the onset of runaway failure) and are calculated as a function of the clear span of the beam, L, and the distance between the extreme fibers of the cross section in compression and tension, d, which includes the slab thickness and depth of the fluted deck for a composite section (Alfawakhiri et al., 2016; Drury and Quiel, 2023b, 2023a). In a standard fire test per ASTM E119, temperatures are measured at a minimum of three sections along the length of the specimen, with four thermocouples at each section as shown in Figure 1. The maximum temperature limit per ASTM E119 is evaluated against the maximum reading among all thermocouples on the steel beam.

Because the bottom flange has the greatest exposure to fire among these three plates, one of its thermocouples often indicates the section's maximum temperature. The top flange temperature, $T_{s,TF}$, typically remains cooler than

that of the web, $T_{s,web}$, and bottom flange, $T_{s,BF}$, calculated as an average of its two thermocouples because its upper surface is in contact with the supported floor slab, thus partially shielding it from heating. $T_{s,BF}$ and $T_{s,web}$ are often similar, with $T_{s,BF}$ being more critical to flexural strength. For the other ASTM E119 thermal limit, a weighted average temperature, $T_{s,E119}$, over a given cross section is calculated as a simple average of all four thermocouple measurements at that section. $T_{s,E119}$ will therefore trend hotter than a true area-weighted average value due to the placement of two thermocouples on the bottom flange and only one each on the other plates (Drury et al., 2020).

The results of standard fire tests are compiled in catalogs such as the UL *Fire Resistance Directory* (2019a). Due to the size limitations of most available furnaces, standard fire tests are usually conducted on floor beam assemblies with shorter spans (10–17 ft) and use a relatively small W-shape section (such as a W8×28 or W12×14). SFRM thicknesses needed for larger sections in actual construction can be calculated using Appendix 4 of the AISC *Specification* (2022), with additional guidance and examples available in ASCE 29-05 (2007) and AISC Design Guide 19 (Ruddy et al., 2003). These resources provide semi-empirical conversion equations based on the relative ratio of cross-sectional area to fire-exposed perimeter between the actual floor beam and the tested specimen from the rated assembly. These methods are implemented as qualification testing per of AISC *Specification* Section A-4.3 and provide a straightforward translation of tested fire resistance to a steel floor beam design.

As an alternative to the prescriptive application of qualification test results, IBC Section 703.2.2.4 (ICC, 2020) permits the use of engineering analysis to demonstrate an

equivalent fire resistance rating as required in Table 601 for an actual member or assembly. To pursue this option, the designer would need adequate thermal and structural information about the setup and outcome of a standard fire test, with which the analysis approach could be validated for the tested specimen. Once validated, the analysis approach could then be applied to a model of the actual assembly (with expected loading and realistic boundary conditions), and a so-called virtual standard fire test would be conducted to determine equivalency to the tested fire resistance rating. However, there are a few significant challenges when attempting to use standard fire test outcomes in this way:

- Per Section 7.4.4.1 of ASTM E119 (2019), the applied flexural loading should represent "the maximum load condition allowed under nationally recognized structural design criteria unless limited design criteria are specified and a corresponding reduced load is applied." Appendix X7 of ASTM E119 states that fire resistance tests have been historically conducted using loads based on maximum allowable stresses. However, the exact load used to test a floor beam assembly is rarely reported in the corresponding fire resistance rating. Variations in assumed material strengths can lead to a range of loads being considered as "the maximum load condition." Also, the flexural design of floor beams at ambient conditions is often governed by serviceability limits rather than by strength. Current application of the ASTM E119 test results in practice do not account for realistic variability of design loading and flexural utilization (which can be calculated as the ratio of applied moment to nominal ambient moment capacity, M/M_n) for realistic floor beam designs. Also, ASTM E119 does not provide any load-based correlation between the thermal and structural performance limits in Table 1.

- The evolution of standard fire testing over time has produced terminology and testing procedures that can be challenging to understand if someone is not intimately familiar with the testing process. Per Table X3.3 of ASTM E119 (2019), hourly ratings for steel floor beams that support concrete slabs can be obtained from four different testing configurations: restrained assembly, unrestrained assembly, restrained beam, and unrestrained beam. Assembly tests also limit thermal transmission through the slab to its unexposed top face, and a restrained beam test does not require the slab edge above the end of the beam to also be restrained (i.e., only the end of the steel beam itself is restrained). Several classifications of hourly ratings can be obtained from a single test when using some of these testing configurations (Berhinig and Alfawakhiri, 2014; Bono, 1970; LaMalva et al., 2020; Ruddy et al., 2003). For example, a single restrained

assembly test can be used to obtain a restrained assembly, unrestrained assembly, and an unrestrained beam rating by applying the varied thermal and structural criteria limits to the single set of test data. An unrestrained beam rating that is extrapolated from a restrained assembly test has slightly different performance limits than that obtained directly from a true unrestrained beam test. Despite this, the published listings of fire resistance ratings for floor beam assemblies (UL, 2019a) do not typically clarify which test configuration was used or which criterion (thermal or structural) was exceeded to obtain a particular hourly rating.

- Per AISC *Specification* Section A-4.3.1 (2022), demonstrating equivalency to a standard fire resistance rating is only permitted via "advanced methods of analysis" as described in Section A-4.2.4c of the same document. These advanced methods typically use finite element (FE) thermal and structural models to evaluate structural fire response. Expertise and project resources (namely, time and budget) are needed to conduct these FE analyses, and the benefits offered by such an approach (either in terms of enhanced performance or fire protection cost savings) must outweigh the costs associated with the design effort. The simple methods of analysis per Section A-4.2.4d, or the recently added critical temperature method per Section A-4.2.4e would be a more accessible tool for tailoring standard fire resistance ratings to realistic floor beam assemblies; however, these approaches are not currently permitted by the AISC *Specification* for this application. Currently, no provisions exist in Section A-4.2.4e related to determining the fire resistance of floor beam assemblies.

In an effort to simplify the determination of equivalent fire resistance for W-shape floor beams, researchers with AISC and AISI performed 16 ASTM E119 standard fire tests in 2015 for which the steel beam was protected with a contoured coating of SFRM (Alfawakhiri et al., 2016). The results of these tests were used to develop the inaugural UL D982 assembly listing (UL, 2019b) and are reproduced in this paper with permission from AISC. All specimens used the same W8×28 section, SFRM thickness, corrugated concrete slab characteristics, and span geometry. Four specimen groups in the following configurations were tested with four specimens each: restrained ends with composite slab (R-C), unrestrained ends with composite slab (U-C), restrained ends with noncomposite slab (R-NC), and unrestrained ends with noncomposite slab (U-NC). The four specimens in each group were each tested with a constant applied flexural load but at a range of magnitudes, inducing a maximum moment, M, ranging from 23–60% of nominal flexural strength, M_n. The results of those tests are used in this paper to illustrate the relationship between flexural response and the increase

in steel beam temperature as a function of applied loading. The results of other quasi-standard tests in the published literature will also be used to further demonstrate this relationship for a wider range of composite beam cross sections, span lengths, slab configurations, and boundary conditions.

The results of the AISC/AISI tests were used as validation for thermo-mechanical FE models in Chapter 6 of the doctoral dissertation by Drury (2022). The reader is directed to that reference for guidance on the implementation of advanced analysis per Section A-4.2.4c of the AISC *Specification* for developing equivalent standard fire resistance. This paper instead demonstrates the application of simple methods of thermal analysis per Appendix 4 of the AISC *Specification* as well as Part 1-2 of Eurocodes 3 and 4 (CEN, 2005, 2008) for predicting critical steel temperatures per the load-dependent relationship. The time at which those critical temperatures are reached under exposure to a standard fire curve could then be used to indicate an equivalent standard fire resistance.

LOAD-DEPENDENT CRITICAL TEMPERATURE RELATIONSHIPS

Existing Specifications

Load-dependent critical temperatures for steel beams are available in current design standards but do not necessarily target composite floor beams. For example, AISC *Specification* Section A-4.2.4e (2022) provides a critical temperature relationship, T_{cr}, for flexural yielding of a continuously braced beam not supporting a concrete slab as a function of

the ratio of applied moment, M, versus the nominal flexural strength due to yielding at ambient temperature, M_n:

AISC *Specification* Equation A-4–23:

$$T_{cr} = 816 - 306 \ln\left(\frac{M}{M_n}\right) \text{(in °F)} \quad (1)$$

Eurocode 3, Part 1-2 (CEN, 2005) provides a similar relationship for critical temperature, T_{cr}, of a generic steel section as a function of initial ambient flexural utilization, M/M_n:

Eurocode 3, Part 1-2, Equation 4.22:

$$T_{cr} = 39.19 \ln\left[\frac{1}{0.9674\left(\frac{M}{M_n}\right)^{3.833}} - 1\right] + 482 \text{ (in °C)} \quad (2)$$

Per both specifications, the values of T_{cr} from Equations 1 and 2 should be applied to the average temperature of the steel cross section, T_s. The plots in Figure 3 show that Equations 1 and 2 both provide similar relationships between T_{cr} and M/M_n for generic steel sections, with the AISC expression providing an approximate 5% conservative value.

Eurocode 4, Part 1-2 (CEN, 2008) permits the application of T_{cr} from Equation 2 as a limit for either T_s or $T_{s,BF}$ in a floor beam that supports a composite slab. The AISC *Specification* does not currently provide an explicit critical temperature relationship for floor beams that support a concrete slab; however, Table A-4.2.4 of the AISC *Specification* provides a flexural retention factor ($k_{cb} = M_{n,T}/M_n$) for composite beams as a function of $T_{s,BF}$ (which is intended to
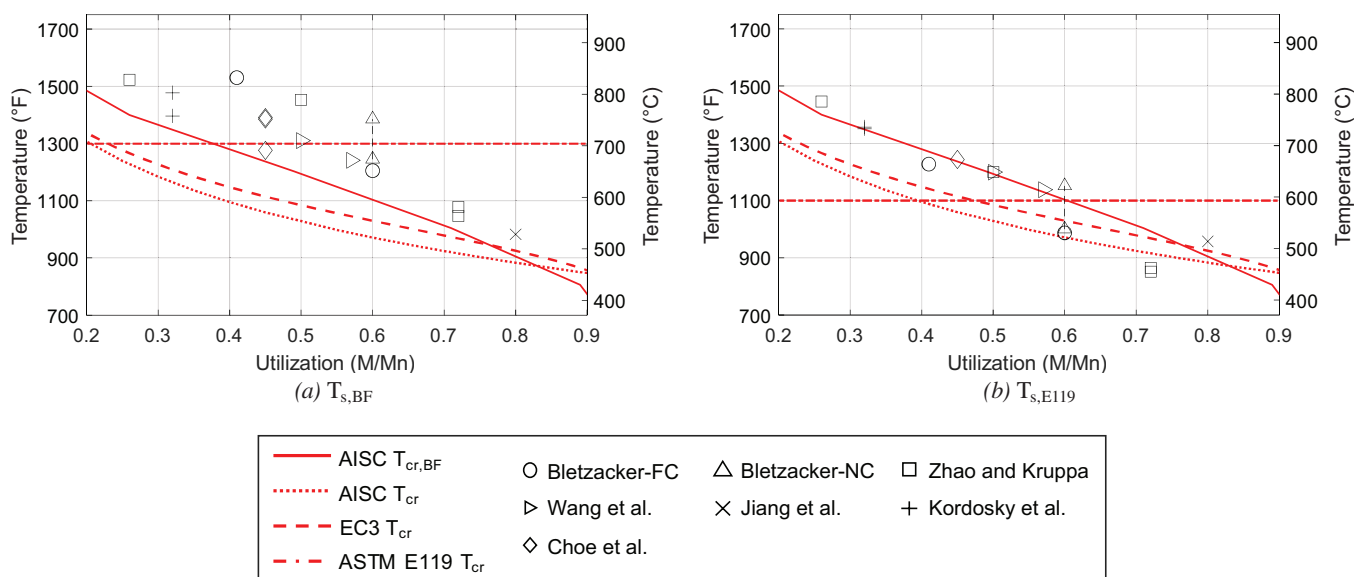

Fig. 3. Critical steel beam temperatures from the existing experimental literature as a function of initial ambient flexural utilization.

represent the maximum temperature of the steel section and govern its flexural resistance). The values in Table A-4.2.4 can be reframed as a function of critical bottom flange temperature, $T_{cr,BF}$, versus flexural utilization, M/M_n, and this relationship is plotted in Figure 3 for comparison. As would be expected, the values for the AISC $T_{cr,BF}$ per Table A-4.2.4 are greater than those for T_{cr} from Equations 1 and 2 up to a flexural utilization of ~75%. These critical temperature curves are compared against the results of quasi-standard fire testing from the published literature in the following section.

Comparison with Published Results of Quasi-Standard Fire Tests

Numerous studies have used a quasi-standard fire test to demonstrate a load-dependent relationship between steel beam temperature and one-way flexural performance of composite and noncomposite floor assemblies, thus supporting the notion that ultimate fire resistance can be correlated to a critical temperature. Table 2 lists seven experimental programs from 1967 to 2020 that tested one-way composite floor beams under a heating regime that either matched or closely resembled a standard fire curve. All tests used varied shear stud layouts to induce a broad range of composite action. Test parameters included both flat and profiled slabs (with varying compressive strengths and concrete unit weights), protected and unprotected steel beams (with varying steel grade, based on their construction era), lengths ranging from 11 to 40 ft (3.35–12.2 m), and varying degrees of axial and rotational end restraint (due to variation in the available support conditions for a particular furnace).

Though limited in some cases by laboratory-specific constraints to prevent damage to the furnace, the flexural failure criteria used for each study was generally similar to that shown in Table 1 and were intended to capture the moment at which the beam would no longer be able to carry the superimposed load. Flexural loading for each test was applied via multiple point loads to induce a maximum bending moment that equaled between 26 and 80% of the ambient (unfactored) moment capacity. Where nominal values were absent in the test reporting, reasonable strength assumptions were made based on the reported properties from material testing. For reference, expected flexural utilization in practice will range from 20 to 60% of the nominal moment capacity, with an upper limit of 70% being reached in rare design circumstances (Newman, 1999).

Nearly all test programs reported a full thermal profile of $T_{s,TF}$, $T_{s,BF}$, and $T_{s,web}$ in the steel beam at failure, with the exception of tests CB-SP and CB-DA-SC per Choe et al. (2020) (which only reported a bottom flange or maximum temperature due to thermocouple malfunctions during testing). The reported temperatures were used to identify

$T_{s,BF}$ and calculate $T_{s,E119}$ at the time of flexural failure per the criteria defined in each study, and the results are plotted as a function of initial ambient flexural utilization in Figure 3. The experimentally measured values of critical $T_{s,BF}$ in Figure 3(a) shows slightly greater dispersion than the corresponding critical $T_{s,E119}$ in Figure 3(b), which suggests that a more consistent result may be obtained when web and top flange temperatures are also incorporated in the critical temperature evaluation. Both plots clearly show that the existing flat critical temperature limits per ASTM E119 are unable to capture the test results across variations in applied loading. Both AISC *Specification* Equation A-4-23 (Equation 1) and the Eurocode critical temperature per Equation 2 provide a good correlation to critical $T_{s,E119}$ across all tests in Figure 3(b). In particular, AISC *Specification* Equation A-4-23 provides a lower bound to most of the test data, with the only exception being the Zhao and Kruppa (1997) results at a flexural utilization ratio of 0.72 (which is above a realistic upper bound of 0.6 for flexural utilization at service levels). The curves for T_{cr} per Equations 1 and 2 provide an unnecessarily conservative prediction of critical $T_{s,BF}$ in Figure 3(a); however, the $T_{cr,BF}$ based on Table A-4.2.4 of the AISC *Specification* provides a reasonably conservative best prediction across all data points. In the next section, these curves will be further evaluated against the results of the aforementioned 16 standard fire tests by Alfawakhiri et al. (2016).

STANDARD FIRE TESTING

Floor Beam Specimen Design

As shown in Figure 4, test specimens consisted of a hot-rolled, W8×28 [50 ksi (345 MPa) yield strength per ASTM A992/A992M (2020)] that supported 2.5 in. (64 mm) of lightweight concrete (LWC) on a 2 in. (51 mm) deep galvanized, fluted metal deck [0.037 in. (0.9 mm) thick]. The steel beams were cut to a total length of 163 in. (4.14 m), and the ends were capped with welded steel plates [12 in. × 8 in. × 0.38 in. (305 mm × 203 mm × 9.7 mm)]. The beam ends were positioned on steel angle bearing supports as shown in Figure 4, leaving a clear span of 154.75 in. (3.93 m). The slab had a total width of 47 in. (1.19 m), and the flutes were oriented perpendicular to the beam span. The LWC had a nominal dry density of 115 pcf (1840 kg/m^3) and a specified minimum compressive strength of 3 ksi (20.7 MPa). A single layer of 6×6 W1.4×W1.4 welded wire reinforcement (WWR) [65 ksi (450 MPa) yield strength per ASTM A1064 (2022)] was placed at mid-thickness of the 2.5 in. concrete topping. The slabs were cured for ~8 months prior to testing, and the relative humidity of the concrete was measured to be less than 70% on the day of testing per ASTM E119 (2019).

Table 2. Summary of Previous Quasi-Standard Fire Tests on One-Way Floor Beam Assemblies

Source	Span	Specimen Design	End Conditions	Protection	Fire Exposure	Initial M/Mn	Flexural Failure Criteria
Bletzacker (1967)	16.8 ft (5.12 m)	Beam: 12W×27 / Slab: 4 in. (102 mm) flat slab / Fully composite (2 tests), Noncomposite (10 tests)	Unrestrained (3 tests), various restraint levels (9 tests)	⅞ in. (22 mm) SFRM on the beam, ½ in. (13 mm) on underside of deck (1.5–2.5 hr rating)	ASTM E119	Constant for each test at 41–60%	"…when the assembly could no longer sustain the vertical design load."
Zhao and Kruppa[a] (1997)	16 ft (4.88 m)	Beam: IPE300 (roughly W12×22) / Slab: 4.7 in. (119 mm) flat slab / Fully composite (4 tests)	Simply supported beam with unrestrained slab	Unprotected (1 test); 1 in. (25 mm) mineral wool on the beam (3 tests)	ISO 834	Constant for each test at 26–72%	Midspan concrete crushing (3 tests); midspan yielding of steel section (1 test)
Wang et al. (2017)	17.3 ft (5.27 m)	Beam: Built-up (roughly W12×26) / Slab: 3.9 in. (99 mm) flat slab / Fully composite (1 test), 50% composite (1 test)	Simply supported beam with unrestrained slab	0.43 in. (11 mm) SFRM on the beam	ISO 834	Constant for each test at 50–57%	Maximum deflection of L/30
Jiang et al. Test SB2 (2017)	16.7 ft (5.09 m)	Beam: Built-up (roughly W12×26) / Slab: 3.9 in. on 3 in. (99 mm on 76 mm) profiled deck / Fully composite (1 test)	Simply supported beam with unrestrained slab	0.39 in. (10 mm) SFRM on the beam	ISO 834	Constant at 80%	Maximum deflection of L/20
Kordosky et al. (2020)	11 ft (3.35 m)	Beam: W12×26 / Slab: 3.25 in. on 2 in. (83 mm on 51 mm) profiled deck / 24% composite (2 tests)	Partially restrained simple connection with unrestrained slab	Unprotected (1 test); 2 hr rated SFRM on the beam (1 test); connections protected for both	ASTM E119	Constant for each test at 32%	Maximum deflection of $L^2/(400d)$ and maximum deflection rate of $L^2/(9000d)$
Choe et al.[b] (2020)	40 ft (12.2 m)	Beam: W18×35 / Slab: 3.25 in. on 3 in. (83 mm on 76 mm) profiled deck / 82% composite (4 tests)	Restrained simple connections with slab restrained (2 tests) or unrestrained (2 tests)	SFRM at 2 hr rating on the beam, 3 hr rating on the connections	Parametric fire that initially emulated ASTM E119[c]	Constant for each test at 45%	Maximum deflection of L/20

a Zhao and Kruppa (1997) Test 5 was partially composite but was halted prematurely due to loading equipment failure; it is therefore excluded.
b Choe et al (2020) Test CB-DA was automatically unloaded prior to reaching significant displacement or a collapse state; it is therefore excluded.
c Constant 3791 Btu/s (4000 kW) heat release rate was targeted—actual temperatures were 266°F (130°C) hotter than ASTM E119 beyond 15 min.

For the eight noncomposite specimens, a single puddle weld was made in every deck flute to the top flange. The nominal ambient plastic moment strength, M_n, of the noncomposite specimen was, therefore, 1,360 kip-in. (153.7 kN-m), which accounts for the contributions of the steel beam only. For the eight composite specimens, a cluster of four shear studs [each ¾ in. (19 mm) in diameter and 3.5 in. (90 mm) in length] were welded through each deck flute [see Figures 5(b) and 5(c)] to the top flange at 12 in. (305 mm) on longitudinal centers, resulting in a fully composite design per the 2010 AISC *Specification* (AISC, 2010; Vinnakota et al., 1988). The nominal moment strength, M_n, of the composite specimens was calculated to be 2,540 kip-in. (287 kN-m) based on an effective slab width of 39.7 in. (1010 mm) (neglecting contributions from the WWR). The W8×28 section is compact at ambient conditions, and the top flange is assumed to have continuous bracing from the slab.

As shown in Figure 5(a), a gap of 1.5 in. (38 mm) was left between the furnace's restraining support and the welded end plate of each specimen. For the restrained configuration in Figure 5(b), the fluted deck was positioned such that concrete would be placed directly against the furnace support. Also, a groove was cut into the deck so that wet concrete would infill the gap between the beam's end plate and the furnace support. This configuration thus provided full bearing restraint to both the beam and slab against outward thrust from thermal expansion and rotation, though
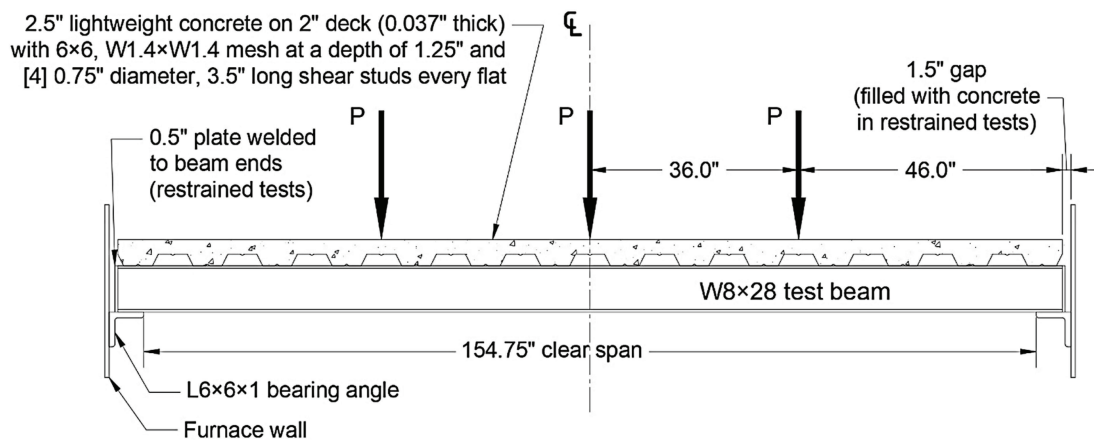
Fig. 4. Side view schematic of the floor beam test specimen, support conditions, and applied loading.

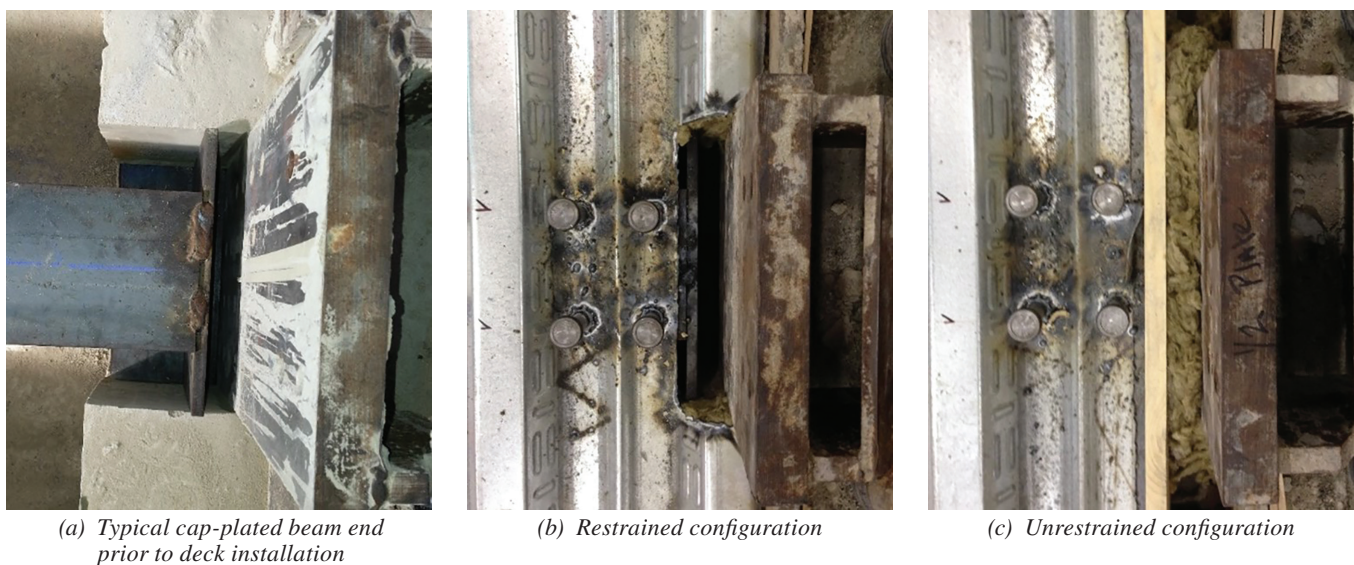| (a) Typical cap-plated beam end prior to deck installation | (b) Restrained configuration | (c) Unrestrained configuration |

Fig. 5. Plan-view photos of the beam end conditions before concrete placement (provided by Farid Alfawakhiri, courtesy of AISC).

no restraint would be provided if the specimen were to pull away from the furnace support. For the unrestrained configuration in Figure 5(c), the deck was trimmed such that the concrete placement would stop short of the furnace wall, with a wood rail used to set the unrestrained edge of the slab. Fiberglass fill was placed into gap between the beam's end plate and the furnace support during concrete placement to prevent accidental infill. Both the wood rail and fiberglass fill were removed prior to testing, preserving the gap and allowing unrestrained expansion and rotation at the ends of the beam and slab.

As shown in Figure 6(a), lightweight SFRM with a nominal dry density of 15 pcf (240 kg/m^3) was applied to the steel beams at a uniform thickness of 1 in. (25 mm). The gap between the top flange and underside of the deck between flutes was also filled with SFRM, as is common practice. No other SFRM was applied to the underside of the fluted deck other than some minor overspray just beyond the edges of the top flange. It should be noted that this SFRM application did not formally target a UL-listed assembly hourly rating and was applied solely to enable comparison between test specimens on the basis of their parametric variation.

Test Setup and Loading

Four specimens were simultaneously tested at a time, side-by-side, in the same furnace using the same heat exposure. As shown in Figure 6(b), the unbonded interface between the longitudinal slab edges of neighboring specimens were covered from above with ceramic wool blankets to mitigate the escape of heat during testing. Prior to SFRM application, four thermocouples were installed on the steel beam cross section per the pattern in Figure 1 at

four equally spaced locations along its length (for a total of 16 thermocouples per beam). Additional thermocouples were placed throughout the furnace to monitor its internal temperature as well as the temperature increase of the slab at a few locations on the top and bottom surfaces and within. The average of those thermocouples for the R-C test group is plotted in Figure 2 and closely follows the ASTM E119 standard fire curve. The average furnace temperature for all other test groups were similarly consistent with the ASTM E119 fire curve and are not plotted for brevity.

Constant flexural loading beyond the specimen self-weight was applied to each beam using concentrated forces at the three locations in Figure 4 via hydraulic cylinders and bearing plates as shown in Figure 6(b). Each of the four specimens in a simultaneous furnace environment was loaded such that the maximum moment at midspan would reach a different percentage of M_n, ranging from 23 to 60% (see Table 3). These moment calculations assumed simple end supports (since significant rotational restraint would not occur at the beam ends under pure flexural loading at ambient conditions) and an effective span length of 159 in. (i.e., the average of the 163 in. total length and the 154¾ in. clear span). It should be noted that the 57 to 60% flexural utilization level was referred to as the "100% load intensity" by the AISC test team (Alfawakhiri et al., 2016) since it represented a maximum expected or service load condition per ASTM E119 (2019) and allowable strength design per the AISC *Specification* (2022). For simplicity, tests herein are labeled using the following nomenclature: restrained or unrestrained (R/U), composite or noncomposite (C/NC), and initial flexural utilization percentage. For example, R-C-60 refers to the restrained, composite beam tested at an initial ambient flexural utilization of 60%.

(a) Typical SFRM-protected beam (showing the longitudinal seam between slabs of adjacent specimens)

(b) Load application

Fig. 6. Pre-test photos of the experimental setup (provided by Farid Alfawakhiri, courtesy of AISC).

Table 3. Summary of Flexural Loading and Corresponding Critical Temperatures per Load-Dependent Relationships in the AISC *Specification* (2022) and Eurocodes 3 and 4 (CEN, 2005, 2008)						
Initial Flexural Utilization, M/M_n		Load P [kips (kN)]	$T_{cr,BF}$ [°F (°C)]		T_{cr} [°F (°C)]	
			AISC *Specification* Table A-4.2.4	EC4 Part 1-2, Section 4.3.4.2.3(4)	AISC *Specification* Equation A-4-23	EC3 Part 1-2, Equation 4.22
Composite	60%	17.8 (79.2)	1100 (593)	1030 (554)	972 (522)	1030 (554)
	48%	14.1 (62.7)	1209 (654)	1096 (591)	1041 (560)	1096 (591)
	36%	10.5 (46.7)	1313 (712)	1177 (636)	1129 (609)	1177 (636)
	24%	6.82 (30.3)	1429 (776)	1288 (698)	1253 (678)	1288 (698)
Noncomposite	57%	8.75 (38.9)	1130 (610)	1047 (564)	990 (532)	1047 (564)
	45%	6.90 (30.7)	1232 (667)	1113 (600)	1058 (570)	1113 (600)
	34%	5.05 (22.5)	1331 (721)	1193 (645)	1146 (619)	1193 (645)
	23%	3.20 (14.2)	1448 (787)	1303 (706)	1270 (688)	1303 (706)

Before any heat was applied, simultaneous testing for four side-by-side specimens was initiated by slowly applying all loads for several minutes until equilibrium was achieved. Heating via the ASTM E119 standard fire curve was then initiated, and the loading was held constant until the specimen was deemed to be no longer capable of sustaining the applied loads. Generally, this meant that the midspan deflection had surpassed the corresponding ASTM E119 criteria per Table 1:

• Composite beam:

  ○ Deflection limit = $L^2/[400(d_{beam}+d_{slab})]$ = 4.81 in. (122 mm)

  ○ Deflection rate limit = $L^2/[9000(d_{beam}+d_{slab})]$ = 0.214 in/min (5.44 mm/min)

• Noncomposite beam:

  ○ Deflection limit = $L^2/(400d_{beam})$ = 7.51 in. (191 mm)

  ○ Deflection rate limit = $L^2/(9000d_{beam})$ = 0.334 in/min (8.48 mm/min)

Upon reaching these limits, the applied loading for that specimen would be removed, although active heating would continue until all four specimens reached the deflection limit states. The midspan deflection of each beam was measured as the increase in distance between the top-of-slab and the underside of the overhead loading frame. These measurements were initiated after the beam was fully loaded and before heating was applied, such that the small amount of deflection in the loading frame due to the reactions from load application would be neglected.

Thermal Response

The temperatures measured in the flanges and web of the four steel beams with the highest loading percentages are plotted in Figure 7 for demonstration—all other specimens with lower loading have very similar steel temperature time histories as those shown here and are thus not provided for brevity. The solid "Avg" curves for $T_{s,TF}$, $T_{s,BF}$, and $T_{s,web}$ represent the mean value of all thermocouples on a corresponding plate over the length of the beam. The dashed curves represent the maximum and minimum recorded temperatures at any single thermocouple on that plate over the length of the beam. The average temperature in each plate is very consistent between specimens. The bottom flange experiences the greatest temperature increase due to its large amount of fire-exposed surface. The web also has a significant amount of exposed surface and is thinner than the flanges, and it therefore develops temperatures that are up to ~200°F (93.3°C) lower than the bottom flange. The difference between maximum and minimum recorded temperature for the bottom flange and web typically does not exceed ~100°F (37.8°C) because they are more uniformly heated. The top flange has a greater range between its minimum and maximum value and develops a lower average temperature because it is in contact with the slab and has less surface area exposed to fire. The top surface of the top flange conducts heat to the slab, which has significant thermal mass and remains cooler than the steel beam throughout the test. Note that the thermal transmission through the slab is not considered to be within the scope of this paper and is therefore not presented; the reader is instead referred to the paper by Alfawakhiri et al. (2016) for that information.

The time at which each specimen reached flexural runaway is also marked in each plot in Figure 7. The temperature time history for U-NC-57 in Figure 7(d) shows a sudden increase in $T_{s,TF}$ at this point, indicating that the SFRM on that plate began to delaminate when the beam lost its flexural resistance. In particular, the maximum temperature for $T_{s,TF}$ converges to the fire curve near the end of the heat application around ~160 min. As will be shown in the next section, U-NC-57 experienced the largest deflection among the four specimens plotted here, which likely enabled the SFRM delamination. It should be noted that U-NC-45 and U-NC-34 also showed similar signs of top flange SFRM delamination at the onset of flexural runaway but at a later time due to their lower level of loading. The $T_{s,TF}$ curve for R-NC-57 in Figure 7(c) also shows indications of minor SFRM delamination (via a sudden uptick in maximum $T_{s,TF}$) but not until 30 min after the loss of flexural resistance. The

$T_{s,TF}$ curve of the other R-NC specimens did not show any noticeable signs of SFRM delamination. Likewise, the steel temperature curves for the composite specimens in Figure 7(a-b) are relatively smooth throughout heating and also indicate no obvious disruption to the integrity of the SFRM.

Figure 8 shows good overall consistency among all 16 specimens regarding their average values of $T_{s,BF}$ and $T_{s,E119}$, calculated across all pertinent thermocouple locations for each specimen. The curves for $T_{s,BF}$ in Figure 8(a) are especially consistent due to the preservation of SFRM integrity on the bottom flange throughout heating, even past the onset of flexural runaway. Due to late onset of SFRM delamination from the top flange, the three gray curves for $T_{s,E119}$ in Figure 8(b) from U-NC specimens with 57%, 45%, and 34% flexural utilization trend higher beyond 120 min than those for all other specimens.
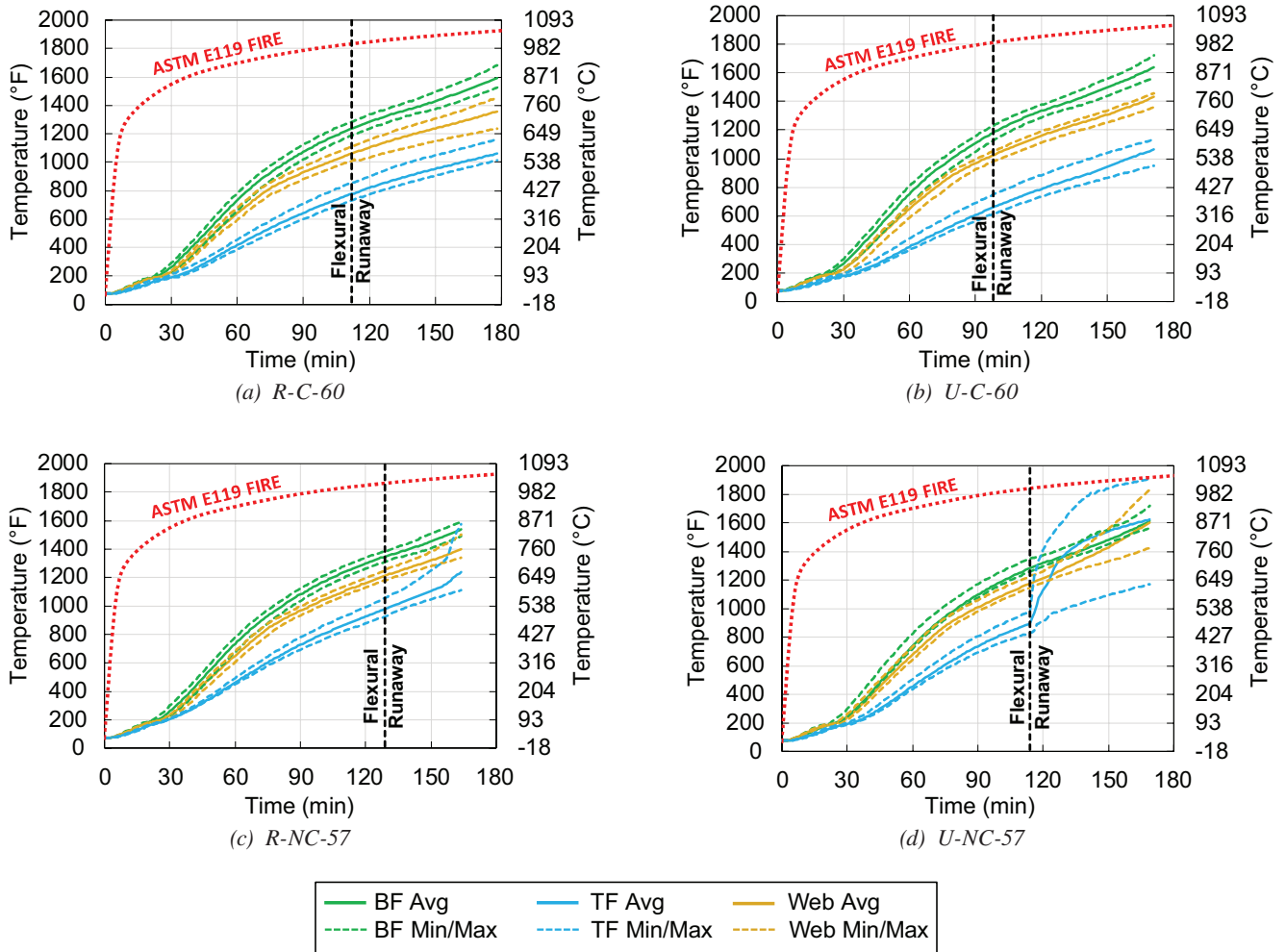

Fig. 7. Measured time histories of $T_{s,BF}$, $T_{s,web}$, *and* $T_{s,TF}$ *for indicated specimens (experimental data provided by Farid Alfawakhiri, courtesy of AISC).*

Flexural Response

The measured time histories of vertical midspan deflection for all 16 tests are plotted in Figure 9, with the ASTM E119 criteria from Table 1 implemented as follows:

- The corresponding ASTM E119 deflection limits for composite and noncomposite specimens are marked as a dashed horizontal line in Figure 9, while an "×" is used to mark the time at which the deflection rate limit is met. Eleven of the 16 specimens met both criteria;

(a) $T_{s,BF}$

(b) $T_{s,E119}$
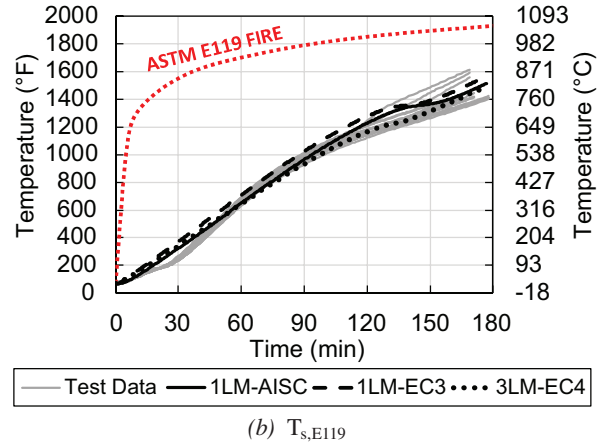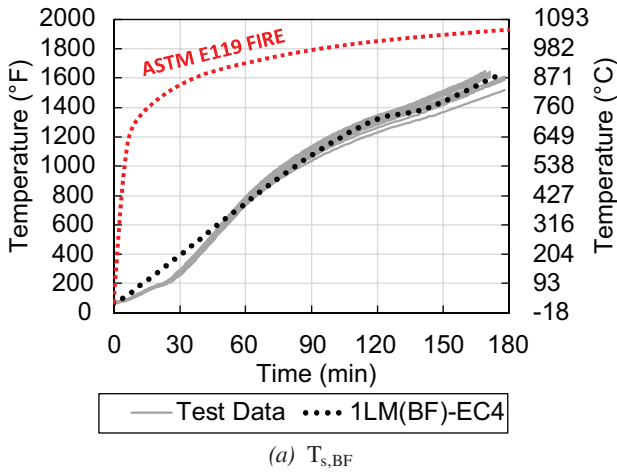
Fig. 8. Comparison of steel temperature time histories from all 16 test specimens (calculated as an average of all longitudinal measurement locations on each beam) against lumped mass temperature predictions (experimental data provided by Farid Alfawakhiri, courtesy of AISC).

(a) Composite

(b) Noncomposite
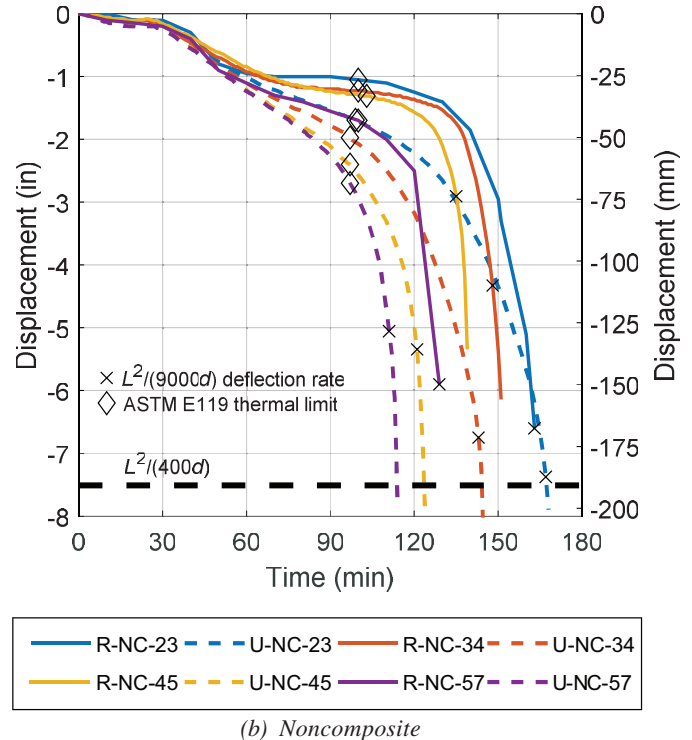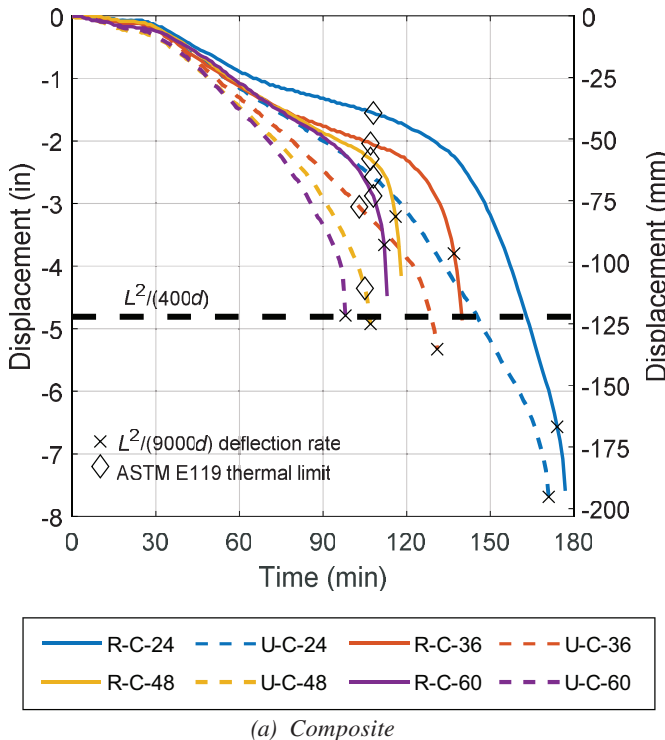
Fig. 9. Measured time histories of vertical midspan deflection for standard fire test specimens (experimental data provided by Farid Alfawakhiri, courtesy of AISC).

restrained specimens R-C-60, R-C-48, R-NC-57, R-NC-45, and R-NC-34 exceeded the deflection rate, but these tests were stopped before reaching the deflection limit to protect the testing equipment from the rapid onset of runaway deflection. The end result for these specimens was deemed to sufficiently signify the loss of flexural resistance.

- The time at which the ASTM E119 thermal limits for $T_{s,MAX}$ or $T_{s,E119}$, whichever came first, are exceeded is marked with a diamond on each curve in Figure 9. The temperatures used to calculate the limits are reflected in the gray curves in Figure 8. All specimens in this test program were governed by the average temperature criteria, $T_{s,E119}$. $T_{s,MAX}$ was typically exceeded in the bottom flange 5–10 min later than $T_{s,E119}$.

The ASTM E119 thermal limit was reached for all specimens between 100 and 110 min, and Figure 9 shows that this flat threshold does not adequately describe the loss of flexural resistance when variations in applied loading are considered. In fact, U-C-60 was the first specimen to exceed both deflection criteria at ~95 min, even though its T_{E119} was still ~50°F (28°C) lower than the corresponding thermal limit. R-C-24 reached flexural runaway just past 175 min, roughly 1 hr after the thermal limit was exceeded. The time needed to reach the thermal and structural limits generally showed closer agreement at higher flexural utilizations, but the deflection limits were reached at significantly longer times when flexural utilization was reduced.

As expected, the restrained specimens exhibited a stiffer initial flexural resistance response in Figure 9 than their unrestrained counterparts at equivalent loads and, as a result, achieved slightly longer times to flexural runaway. All specimens show relatively similar initial deflection down to a value of ~1 in., after which the deflection rate for restrained specimens becomes shallower due to the growing influence of restraint forces and hogging moment at the beam ends. After they have stiffened and developed additional restraining stresses, however, the restrained specimens then develop a rapid increase in deflection rate toward runaway failure at lower magnitudes of deflection than in the unrestrained cases. The unrestrained specimens exhibit a more gradual overall deflection response as their temperatures increases, with the deflection rate accelerating toward runaway only in the last few minutes before the loading was stopped.

Observations from Post-Test Inspection

Photos from the post-fire inspection of each group of specimens are shown in Figures 10 and 11. Photos taken from above show that all four specimens in each group exhibited similar ultimate deflected shapes regardless of initial flexural utilization, even though flexural resistance was exceeded at different times according to the applied load level. Figures 10(a) and 11(a) clearly show that the hogging moment at the ends of the restrained specimens caused significant transverse cracking in the top of the composite slab [Figure 10(b)] as well as plastic hinging at the end of the beam [Figures 10(c) and 11(b)]. Despite lacking a true connection, the restrained specimens were able to develop these hogging moments at their ends due to the compressive reaction of the end plates against the furnace supports to resist axial thermal expansion. As shown previously in Figure 7, the bottom flange and web undergo a larger temperature increase and would therefore experience more restraint of thermal expansion than the top flange and slab. Larger horizontal compressive reactions near the bottom of the beam would produce an eccentricity at the contact of the end plate against the support, thereby inducing the hogging moment (i.e., inducing upward rotation) that is observed at the ends of the restrained specimens.

For the unrestrained specimens in Figures 10(d) and 11(c), the gap between the furnace support and the ends of the specimens allowed thermal expansion and end rotation; therefore, there was no noticeable post-test transverse cracking or plastic hinging near the unrestrained ends. The final parabolic deflected shapes of the unrestrained specimens in Figures 10(f) and 11(d) resemble the anticipated deflected shapes for idealized simply supported boundary conditions intended by the standard test setup. The U-NC specimens in Figure 11(c) show very little slab cracking due to the relatively low engagement of the noncomposite slab; however, increased deflections due to lower stiffness caused some observable SFRM delamination, particularly at the top flange [see Figure 11(d)]. This observation supports the onset of rapid temperature increase in the top flange after flexural runaway as shown previously for U-NC-57 in Figure 7(d). Conversely, Figures 10(c) and 10(f) show that none of the composite beam specimens experienced noticeable SFRM loss prior to the loss of flexural resistance.

As shown in Figure 10(e), the U-C specimens developed large lengthwise longitudinal cracks just beyond the width of the bearing plates for point load application. No transverse support was provided to the slab edges in these tests, and it should be noted that longitudinal cracking would not be expected in an actual building with a continuous slab that spanned transversely to the next parallel floor beam. In these tests, the longitudinal cracking of the U-C specimens was likely caused by differential thermal expansion between the beam and unrestrained composite slab (which was significantly cooler than the beam due to its larger thermal mass, lower thermal conductivity, and lower ratio of heated area to overall volume). The hotter beam is, therefore, longitudinally restrained by the cooler slab due to their composite interface. The unrestrained slab, as a result, develops nonuniform transverse stress distribution, and the
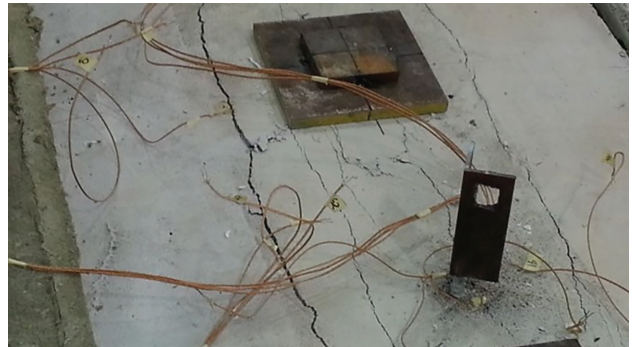
(a) R-C specimens from above

(d) U-C specimens from above

(b) R-C slab edge transverse cracking

(e) U-C longitudinal slab cracking

(c) R-C specimens from below

(f) U-C specimens from below

Fig. 10. Post-test photos of the composite specimens (provided by Farid Alfawakhiri, courtesy of AISC).

longitudinal cracks indicate a shear plane in the transition between the highly composite center portion and the less restrained outer portions of the slab.

Critical Temperature Verification

The plots in Figure 12 are similar to those in Figure 3, but the data points from previous experimental studies have been replaced with those derived from the standard fire tests of the 16 specimens. The following critical temperatures are taken for each specimen at the time at which the specimen reached the ASTM E119 deflection rate limit (again, marked with an "×" in Figure 9): (a) maximum $T_{s,BF}$ measured at any location along the length of the beam and (b) maximum $T_{s,E119}$ at any one of the three cross-section locations along the length of the beam, as shown in Figure 1(b). Both plots again show that the ASTM E119 flat critical temperature limits do not accurately capture the effects of applied

loading on structural resistance to standard fire exposure. The best correlation for those limits is observed at 48% initial flexural utilization, which is consistent with the fact that the 1100°F (593°C) critical temperature limit for $T_{s,E119}$ correlates to an approximate 50% reduction in steel yield strength (AISC, 2022; CEN, 2005). The AISC *Specification* flexural retention factor provides a conservative lower bound across all critical $T_{s,BF}$ in Figure 12(a). AISC *Specification* Equation A-4-23 (Equation 1) and the Eurocode critical temperature per Equation 2 (which are intended to represent the temperature of the entire steel member) logically provide a closer correlation to critical $T_{s,E119}$ across all tests in Figure 12(b) but provide an unnecessarily conservative prediction of critical $T_{s,BF}$ in Figure 12(a).

It should be noted that the noncomposite specimens consistently exhibited ~100°F (37.8°C) higher critical temperature at the onset of flexural runaway than their composite

(a) R-NC specimens from above

(c) U-NC specimens from above

(b) R-NC specimens from below

(d) U-NC specimens from below

Fig. 11. Post-test photos of the noncomposite specimens (provided by Farid Alfawakhiri, courtesy of AISC).

Table 4. Summary of Standard Fire Resistance Times (in minutes) Based on Thermal and Structural Test Results							
Initial Flexural Utilization, M/M_n		Limit: ASTM E119 Deflection Rate		Limit: AISC $T_{cr,BF}$		Limit: AISC T_{cr}	
		R-Test Deflection	U-Test Deflection	R-Test $T_{s,BF}$	U-Test $T_{s,BF}$	R-Test $T_{s,E119}$	U-Test $T_{s,E119}$
Composite	60%	112	98	93	89	96	93
	48%	116	107	104	100	101	101
	36%	137	131	123	116	118	115
	24%	174	171	161	141	144	140
Noncomposite	57%	129	114	95	92	93	90
	45%	139	123	104	102	99	96
	34%	151	144	124	117	114	108
	23%	163	167	154	139	138	132

counterparts. It is likely that the noncomposite slab made a non-negligible contribution to the flexural resistance of those beams; however, the loading applied to each noncomposite beam was calculated as a percentage of the beam's plastic moment capacity only. Excess capacity relative to the assumed level of initial flexural utilization would therefore translate into a higher critical temperature at the onset of flexural runaway. This design concept indicates that the design flexural utilization (as plotted) is often a conservative estimate of noncomposite strength, meaning that critical temperature relationships as a function of flexural utilization for composite beams can be used to conservatively estimate noncomposite critical temperature relationships.

Table 4 summarizes the times at which each specimen reached the ASTM E119 deflection rate limit. Also shown are the times at which the recorded average $T_{s,BF}$ and $T_{s,E119}$ from each specimen (plotted previously in Figure 8) reach their corresponding AISC critical temperature from Table 3. The relationship between these fire resistance times is visualized in Figure 13 as a correlation plot, with thermally predicted values on the vertical axis and deflection-based values on the horizontal axis. Points that fall below the 1:1 line indicate that the thermal prediction of fire resistance is lower (or conservative) relative to the deflection-based resistance. The banded lines indicate a percentage of increase or decrease in thermally predicted fire resistance versus the deflection-based resistance.

(a) $T_{s,BF}$

(b) $T_{s,E119}$

AISC $T_{cr,BF}$ — — — EC3 T_{cr} ⬤ R-C ⬤ U-C
·········· AISC T_{cr} —·—·— ASTM E119 T_{cr} 🟨 R-NC 🟪 U-NC

Fig. 12. Critical steel temperatures for flexural failure of standard fire test specimens as a function of initial ambient flexural utilization.

Figure 13 shows that imposing the AISC *Specification* critical temperature limits on the experimental measurements of $T_{s,BF}$ and $T_{s,E119}$ provides similarly conservative fire resistance predictions relative to the onset of flexural runaway. Fire resistances based on critical temperatures for noncomposite specimens are more conservative, again because the calculation of initial flexural utilization neglected any flexural contributions from the slab. Fire resistance times based on critical temperatures for the composite specimens show good agreement with flexural runaway (with most no more than 15% conservative), while those for noncomposite specimens are 15–30% conservative. As shown in Figure 12(b), the Eurocode 3 critical temperatures are slightly greater than the AISC *Specification* Equation A-4-23 curve and would, therefore, be expected to provide even closer predictions of flexural runaway under standard fire exposure when used with $T_{s,E119}$. Altogether, these results suggest that these critical temperature limits can provide reasonably conservative estimates of one-way flexural resistance to standard fire exposure for this type of floor beam assembly.

SIMPLIFIED METHODS FOR CRITICAL TEMPERATURE ANALYSIS

There are currently no provisions in the AISC *Specification* for determining critical temperature per Section A-4.2.4e for floor beams. Also, there are no direct means per Section A-4.3.1 for achieving equivalence to a standard fire resistance rating other than through an advanced analysis method outlined in Section A-4.2.4c. Typically, this analysis would use a 2D or 3D finite element (FE) mesh (Drury and Quiel, 2023b; Franssen and Gernay, 2017; Selden and Varma, 2016) of the composite or noncomposite beam cross section. Rather than resorting to such advanced analysis methods (which require greater effort and expertise by the analyst), the temperature increase in a protected W-shape floor beam cross section can instead be predicted using lumped mass (LM) thermal analysis techniques, which are classified as simple analysis methods in Section A-4.2.4d. The W-shape beam section can be represented as a single LM (AISC, 2022; Buchanan and Abu, 2017; CEN, 2005; Gamble, 1989), or multiple LMs can be used to represent the flange and web plates (CEN, 2008; Drury et al., 2020, 2021; Ghojel and Wong, 2005). These methods can be implemented in spreadsheets or other simple mathematical solvers and have been shown to provide conservatively accurate predictions of thermal behavior in experimental testing of composite floor beams (Drury et al., 2020, 2021; Drury and Quiel, 2023b). The simplified LM calculations presented herein are demonstrated as capable tools for predicting critical temperature for floor beams while simultaneously providing a means of calculating equivalence to ASTM E119 hourly fire resistance ratings.

Single Lumped Mass Methods

The following calculations from the AISC *Specification* and Part 1-2 of Eurocode 3 represent the steel beam section as a single lumped mass (1LM) that has uniform temperature
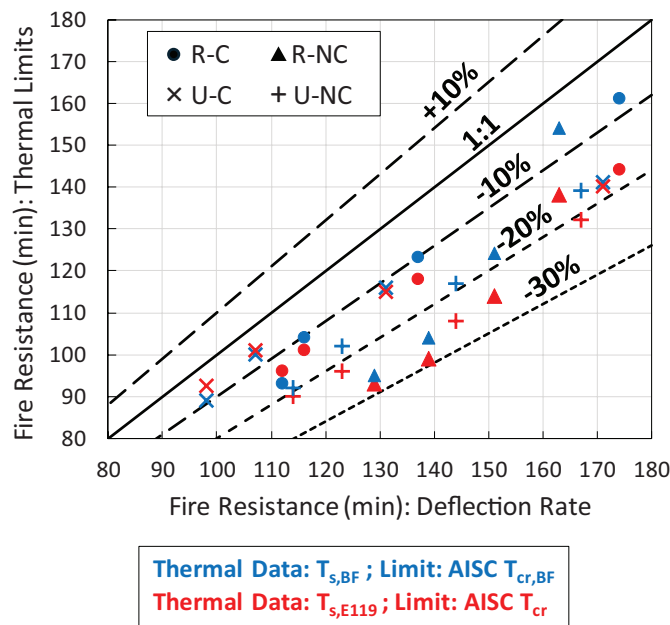

Fig. 13. *Correlation plot of standard fire resistance times based on thermal and structural test results.*

T_s and is uniformly coated with a contoured constant thickness of fire protective insulation:

AISC *Specification* Equation C-A-4-7 (U.S. units):

$$T_{s,i} = T_{s,i-1} + \frac{k_{p,i}}{d_p} \left[\frac{T_{f,i} - T_{s,i-1}}{c_{s,i}\left(\dfrac{W}{D}\right) + \dfrac{c_{p,i}\rho_{p,i}d_p}{2(144)}} \right] \Delta t \quad (3)$$

Eurocode 3, Part 1-2, Equation 4.27 (metric units):

$$T_{s,i} = T_{s,i-1} + \frac{k_{p,i}}{d_p} \left[\frac{T_{f,i} - T_{s,i-1}}{c_{s,i}\left(\dfrac{W}{D}\right) + \dfrac{c_{p,i}\rho_{p,i}d_p}{3}} \right] \Delta t \quad (4a)$$
$$- (e^{\phi_i/10} - 1)(T_{f,i} - T_{f,i-1})$$

$$\phi_i = \frac{c_{p,i}\rho_{p,i}d_p}{c_{s,i}\left(\dfrac{W}{D}\right)} \quad (4b)$$

where

A_s = total cross-sectional steel area, ft^2 (m^2)

D = heated perimeter, in. (mm)

$T_{f,i}$ = temperature of the fire at time step i, °F (°C)

$T_{s,i}$ = temperature of the steel section at time step i, °F (°C)

W = weight (mass) per unit length, lb/ft (kg/m) = $\rho_s A_s$

$\dfrac{W}{D}$ = section factor for the fire exposed surfaces

$c_{s,i}$ = steel specific heat at time step i, Btu/lb-°F (J/kg-K)

$c_{p,i}$ = fire protection specific heat at time step i, Btu/lb-°F (J/kg-K)

d_p = fire protection thickness, in. (m)

i = time step number

$k_{p,i}$ = fire protection thermal conductivity at time step i, Btu/ft-sec-°F (W/m-K)

Δt = time step increment (sec)

$\rho_{p,i}$ = fire protection density at time step i, lb/ft^3 (kg/m^3)

ρ_s = steel density = 490 lb/ft^3 (7,850 kg/m^3)

Note that the original form of Equation 4 from Eurocode 3 has been reformatted to be similar to Equation 3 (which is taken from the AISC *Specification)* to facilitate a direct comparison. The two 1LM calculation approaches are similarly based on the assumption that the outer surface of the protection layer is equal to the fire temperature, and the inner surface of the protection layer is equal to the steel temperature. Eurocode includes an additional reduction in $\Delta T_{s,i}$ at every time step as a function of the change in applied fire temperature $\Delta T_{f,i}$ during that step. In this way, the Eurocode formulation slightly reduces $\Delta T_{s,i}$ when the fire temperature is growing at a rapid rate.

The value of D for both formulations is calculated using the inner perimeter of the contoured fire protection per Eurocode 3 (CEN, 2005). For a W-shape floor beam section that supports a slab, D is calculated as follows:

$$D = 2d + 3b_f - 2t_w \quad (5)$$

In this study, the thermal properties of the steel and SFRM are realistically considered as a function of their increasing temperature. To avoid the need for iteration at each time step, these properties can be calculated using temperatures obtained at the previous time step (Drury et al., 2020; Gamble, 1989), as long as the time step remains sufficiently small. The following calculations are made to obtain the thermal properties of the steel and SFRM at each time step i:

- $c_{s,i}$ for the steel section is calculated as a function of $T_{s,i-1}$ using the temperature-dependent relationship in Eurocode 3, Part 1-2 (CEN, 2005).

- $c_{p,i}$, $k_{p,i}$, and $\rho_{p,i}$ for the fire protection are calculated as a function of the assumed temperature of the fire protection material, $T_{p,i}$, taken as $T_{p,i} = (0.9T_{s,i-1} + 0.1T_{f,i-1})$ using the mean value of the empirical relationship per Khorasani et al. (2015) for standard, low-density SFRM (with a density of approximately 15 pcf (240 kg/m^3)].

For this study, all LM thermal calculations are performed using $\Delta t = 30$ sec in accordance with Eurocode 3, Part 1-2 (CEN, 2005), which was sufficiently small to obtain convergent solutions as well as good agreement with the experimentally measured $T_{s,E119}$ [see Figure 8(b)]. The use of weighted average $T_{p,i} = (0.9T_{s,i-1} + 0.1T_{f,i-1})$ to calculate the temperature-dependent SFRM properties was also determined based on good agreement with the experimental data. The stronger weighting of the steel temperature reflects the presumed shape of the thermal gradient that develops over the thickness of the SFRM when exposed to fire. Specifically, the high temperature at the fire-exposed outer SFRM surface would exhibit an approximately exponential decay over the SFRM thickness toward the protected inner surface of the steel section. More research is needed to demonstrate a broad applicability of this approach for calculating temperature-dependent SFRM thermal properties in these 1LM methods. Figure 8(b) shows that the simpler AISC formulation provides a slightly closer prediction of the experimentally measured $T_{s,E119}$ than the EC3 formulation when using the same material inputs.

Multiple Lumped Mass Method

As shown in Figure 7, the bottom flange, top flange, and web will realistically develop different temperatures due to differences in fire-exposed perimeter; the assumption of a single uniform T_s for the entire cross section is therefore a

significant simplification. As an alternative, the steel section can be subdivided into multiple lumped masses for which a thermal calculation can be made at each time step (Drury et al., 2020, 2021; Ghojel and Wong, 2005). Part 1-2 of Eurocode 4 adapts the equations from Part 1-2 of Eurocode 3 such that each flange and the web are considered as separate LMs:

Eurocode 4, Part 1-2, Equation 4.8 (metric units):

$$T_{s,j,i} = T_{s,j,i-1} + \frac{k_{p,i}}{d_{p,j}} \left[\frac{T_{f,i} - T_{s,j,i-1}}{c_{s,j,i} \left(\frac{W_j}{D_j} \right) + \frac{c_{p,j,i}\, \rho_{p,j,i}\, d_{p,j}}{3}} \right] \Delta t \quad (6a)$$

$$- (e^{\phi_{j,i}/10} - 1)(T_{f,i} - T_{f,i-1})$$

$$\phi_{j,i} = \frac{c_{p,j,i}\, \rho_{p,j,i}\, d_{p,j}}{c_{s,j,i} \left(\frac{W_j}{D_j} \right)} \qquad (6b)$$

where

j = plate component designation (*BF, TF, web*)

$T_{s,j,i}$ = temperature of plate component j at time step i, °C

$\dfrac{W_j}{D_j}$ = section factor for the fire exposed surfaces of plate component j

In the Eurocode 4 approach, the section factor W_j/D_j for each flange is calculated using the following inputs:

Bottom flange: $\quad D_{BF} = 2t_f + 2b_f \qquad (7a)$

$$A_{s,BF} = b_f t_f \qquad (7b)$$

Top flange: $\quad D_{TF} = 2t_f + b_f \qquad (7c)$

$$A_{s,TF} = b_f t_f \qquad (7d)$$

Again, note that the original form of Equation 6 from Eurocode 4 has been reformatted to be similar to Equation 3 for comparison. Figure 8(a) shows very good agreement between the experimental measurements of $T_{s,BF}$ and that predicted by the Eurocode 4 approach for the *BF* as a single lumped mass (1LM). If the beam depth does not exceed 20 in. (500 mm), Eurocode 4 notes that the temperature of the web can be taken as equal to that of the bottom flange for simplification:

$$T_{s,web,i} \approx T_{s,BF,i} \qquad (8)$$

The average temperature of the W-shape cross section can then be calculated as an area-weighted average among the three plate lumped masses (3LM):

$$T_{s,AVG,i} = \sum_{j=1}^{3} T_{s,j,i} \left(\frac{A_{s,j}}{A_s} \right) \qquad (9)$$

Figure 8(b) shows that $T_{s,AVG}$ per the 3LM approach in Equation 9 provides an even closer prediction of the experimentally measured $T_{s,E119}$ than the 1LM approaches.

Sensitivity to SFRM Thermal Properties

It should be emphasized that the accuracy of these LM predictions is dependent on the temperature-dependent relationships used to obtain thermal properties of the steel and fire protection materials. For comparison, two additional predictions of T_s are made using Equation 3 from the AISC *Specification* but with two alternative temperatures used to calculate the SFRM thermal properties at every time step via the Khorasani et al. (2015) mean value relationships for $c_{p,i}$, $k_{p,i}$, and $\rho_{p,i}$: $T_{p,i} = 500$°C (as permitted by the AISC *Specification* as a simplification), and $T_{p,i} = T_{s,i-1}$ (representing a lower-bound simplification). Figure 14 shows that these alternate approaches can provide predictions of $T_{s,E119}$ that are either slightly higher or lower, respectively, versus the experimental data or the 1LM-AISC prediction of T_s using $T_{p,i} = (0.9T_{s,i-1} + 0.1T_{f,i-1})$ (reproduced from Figure 8). The user should exercise caution and potentially seek opportunities for preliminary experimental validation when applying these methods in practice to calculate equivalent standard fire resistance. Also note that some of the gray curves representing the experimental data begin to
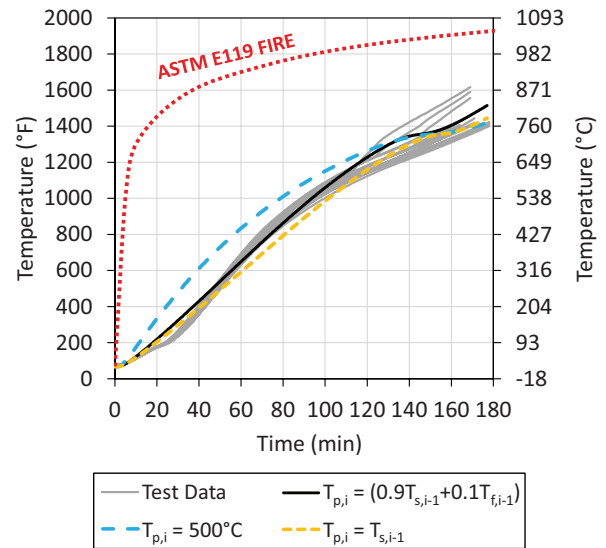

Fig. 14. Comparison of time histories for $T_{s,E119}$ *from all 16 specimens (calculated as an average of all longitudinal measurement locations for each beam) against 3 iterations of the AISC Specification 1LM prediction for* T_s *(with different values of* T_p *used to determine the SFRM thermal properties at each time step) (experimental data provided by Farid Alfawakhiri, courtesy of AISC).*

Table 5. Comparison of Standard Fire Resistance Times (in minutes): Flexural Performance of Tested Specimens Versus Thermal LM Predictions of Load-Dependent Critical Temperature.						
Initial Flexural Utilization, M/M_n	Limit: ASTM E119 Deflection Rate		Limit: AISC $T_{cr,BF}$	Limit: AISC T_{cr}	Limit: EC3 T_{cr}	
	R-Test Deflection	U-Test Deflection	1LM EC4 $T_{s,BF}$	1LM AISC T_s	1LM EC3 T_s	3LM EC4 $T_{s,AVG}$
Composite 60%	112	98	93	91	91	101
48%	116	107	105	98	98	110
36%	137	131	119	108	107	122
24%	174	171	149	123	122	146
Noncomposite 57%	129	114	96	93	92	104
45%	139	123	108	100	100	113
34%	151	144	122	110	109	125
23%	163	167	151	126	124	148

trail upward beyond 120 min, due to likely SFRM loss after the onset of flexural runaway.

Critical Temperature Predictions

The load-dependent critical temperature relationships from Table 3 can be applied to the various LM predictions of T_s to predict the standard fire resistance. Table 5 compares these predictions against the fire resistance times corresponding to the onset of flexural runaway in each test (which are reproduced from Table 4). Similar to Figure 13, the relationship between these fire resistance times is visualized in Figure 15 as a correlation plot, with LM thermal predictions on the vertical axis and deflection-based values from the tests on the horizontal axis. Points that fall below the 1:1 line indicate that the LM prediction of fire resistance is lower (or conservative) relative to the deflection-based resistance. Due to the enhanced accuracy of the Eurocode 4 LM predictions of steel temperature (see Figure 8), the predicted fire resistance times based on those calculations (plotted in red and blue in Figure 15) are similarly conservative as those based on the experimentally measured temperatures in Figure 13. Fire resistances based on the 1LM methods (plotted in green and gold in Figure 15) are slightly more conservative than those in Figure 13 because their predictions of T_s are more conservative relative to the experimentally measured T_s (see Figure 8).

CONCLUSIONS

The results of this study demonstrate that simplified thermal analysis methods can be combined with load-dependent critical temperature relationships to conservatively predict the standard fire resistance of W-shape floor beam assemblies at flexural runaway. In practice, a designer would be able to iteratively perform these calculations to determine the thickness and material properties of SFRM needed to achieve an equivalent targeted hourly fire resistance rating
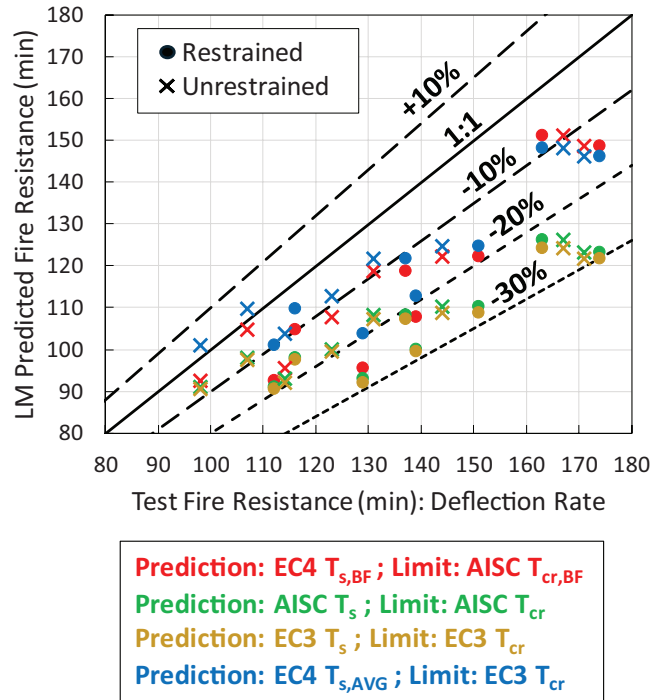

Fig. 15. Correlation plot of standard fire resistance times from structural test results versus thermal LM predictions of load-dependent critical temperature.

for a given floor beam section. The design of floor beams is often governed by deflection-based serviceability criteria rather than strength criteria; the load-dependent critical temperature relationships per the AISC *Specification* and Part 1-2 of Eurocodes 3 and 4 therefore offer the ability to tailor an equivalent standard fire resistance to the actual flexural utilization of the member.

The following conclusions can be drawn from this study:

- Based on the results of standard fire testing by AISC/ AISI in 2015 (as well as other quasi-standard fire test results in the published literature), the critical value of bottom flange temperature, $T_{s,BF}$, at the onset of flexural runaway can be conservatively predicted using the load-dependent values of $T_{cr,BF}$ in AISC *Specification* Table A-4.2.4 (2022). Likewise, the critical value of $T_{s,E119}$ (i.e., the average steel section temperature based on the thermocouple placement during an ASTM E119 standard fire test) at the onset of flexural runaway can be conservatively predicted using the load-dependent relationships of T_{cr} per Equation 4.22 from Eurocode 3, Part 1-2 (CEN, 2005) as well as AISC *Specification* Equation A-4-23.

- Based on the standard fire test data presented in this paper, these load-dependent critical temperature relationships for standard fire resistance are robust for SFRM-protected W8×28 floor beam assemblies that are restrained or unrestrained to thermal expansion, with composite or noncomposite reinforced concrete slabs (cast on corrugated metal decking). The quasi-standard test results in the published literature indicate that these critical temperature relationships may also be robust for section depths ranging from W8 to W18, the inclusion of shear tab connections (rather than unrealistic end-plate bearing connections, which are used in standard fire tests), the implementation of flat slabs (rather than those cast on corrugated metal decking), the material property details of the slab's concrete, unprotected steel beam sections (i.e., with no applied passive fire protection), variation in steel beam yield strength (with nominal ranging from 36–50 ksi), and span lengths ranging from 11 to 40 ft.

- The 3LM predictions of steel temperature for each flange and the web under standard fire exposure per Eurocode 4 slightly outperformed 1LM predictions of T_s for the entire section per Eurocode 3 and the AISC *Specification*. However, all LM predictions provided reasonably accurate and conservative estimations of standard fire resistance compared to those corresponding to flexural runaway of the AISC specimens tested to ASTM E119. The quality of these LM predictions depends on the temperature-dependent relationships that are used to calculate thermal properties of the

steel and fire protection materials at each time step. Simplifying approximations were shown to be capable of conservatively predicting the steel temperature increase under standard fire exposure.

REFERENCES

AISC (2010), *Specification for Structural Steel Buildings,* ANSI/AISC 360-10, American Institute of Steel Construction, Chicago, Ill.

AISC (2022), *Specification for Structural Steel Buildings,* ANSI/AISC 360-22, American Institute of Steel Construction, Chicago, Ill.

Alfawakhiri, F., Carter, C.J., Berhing, R.M., Zeeveld, P., Hervey, F.E., and Woods, L.C. (2016), "The Effects of Load Intensity and Restraint on the Fire Resistance of Steel and Composite Beams," *9th International Conference on Structures in Fire SiF'16*, Princeton University, N.J.

ASCE (2007), *Standard Calculation Methods for Structural Fire Protection (ASCE/SEI/SFPE 29-05)*, American Society of Civil Engineers, Reston, Va.

ASCE (2020), *Performance-Based Structural Fire Design: Exemplar Designs of Four Regionally Diverse Buildings Using ASCE 7-16, Appendix E*, American Society of Civil Engineers, Reston, Va., doi: 10.1061/9780784482698.

ASTM (2019), *Test Methods for Fire Tests of Building Construction and Materials*, ASTM E119-19, ASTM International, West Conshohocken, Pa., doi: 10.1520/ E0119–19.

ASTM (2020), *Standard Specification for Structural Steel Shapes*, ASTM A992–20, ASTM International, West Conshohocken, Pa., doi: 10.1520/A0992_A0992M-20.

ASTM (2022), *Standard Specification for Steel Wire and Welded Wire Reinforcement, Plain and Deformed, for Concrete*, ASTM A1064-22, ASTM International, West Conshohocken, Pa., doi: 10.1520/A1064_A1064M-22.

Berhinig, R.M. and Alfawakhiri, F. (2014), "New Fire Resistance Test for Loaded Unrestrained Beams," *ASCE/SEI Structures Congress*, American Society of Civil Engineers, Boston, Mass., pp. 1175–1184, doi: 10.1061/9780784413357.106.

Bletzacker, R.W. (1967), "Fire Resistance of Protected Steel Beam Floor and Roof Assemblies as Affected by Structural Restraint," *Symposium on Fire Test Methods—Restraint & Smoke 1966 (ASTM STP 422)*, ASTM International, West Conshohocken, Pa., pp. 63–90., doi: 10.1520/STP41306S.

Bono, J.A. (1970), "New Criteria for Fire Endurance Tests," *Fire Test Performance (ASTM STP 464)*, ASTM International, West Conshohocken, Pa., pp. 106–126, doi: 10.1520/STP44715S.

BSI (1987), *Fire Tests on Building Materials and Structures—Part 21: Methods for Determination of the Fire Resistance of Load-Bearing Elements of Construction*, BS 476-21:1987, British Standards Institute (BSI), London, UK.

BSI (2008), *Fire Tests on Building Materials and Structures. Part 10. Guide to the Principles, Selection, Role, and Application of Fire Testing and Their Outputs.*, BS 476-10:2009, British Standards Institute (BSI), London, UK.

Buchanan, A.H. and Abu, A. (2017), *Structural Design for Fire Safety*, 2nd Ed., John Wiley & Sons Inc., Chichester, West Sussex, UK.

CEN (2005), *EN 1993-1-2:2005 Eurocode 3: Design of Steel Structures—Part 1-2: General Rules—Structural Fire Design*, EN 1993–1-2:2005, European Committee for Standardization, Brussels, Belgium.

CEN (2008), *EN 1994–1-2:2005 Eurocode 4: Design of Composite Steel and Concrete Structures—Part 1-2: General Rules—Structural Fire Design*, European Committee for Standardization, Brussels, Belgium.

CEN (2009), *EN 1991–1-2:2002 Eurocode 1: Actions on Structures—Part 1-2: General Actions—Actions on Structures Exposed to Fire*, European Committee for Standardization, Brussels, Belgium.

Choe, L., Ramesh, S., Grosshandler, W., Hoehler, M., Seif, M., Gross, J., and Bundy, M. (2020), "Behavior and Limit States of Long-Span Composite Floor Beams with Simple Shear Connections Subject to Compartment Fires: Experimental Evaluation," *Journal of Structural Engineering*, Vol. 146, No. 6, p. 04020088, doi: 10.1061/(ASCE)ST.1943–541X.0002627.

Drury, M.M. (2022), *Critical Temperature Relationships for the Performance-Based Design of Realistically-Restrained Steel Composite Floor Assemblies*, Ph.D. Thesis, Lehigh University, Bethlehem, Pa.

Drury, M.M., Kordosky, A.N., and Quiel, S.E. (2020), "Structural Fire Resistance of Partially Restrained, Partially Composite Floor Beams, II: Modeling," *Journal of Constructional Steel Research*, Vol. 167, p. 105946, doi: 10.1016/j.jcsr.2020.105946.

Drury, M.M., Kordosky, A.N., and Quiel, S.E. (2021), "Robustness of a Partially Restrained, Partially Composite Steel Floor Beam to Natural Fire Exposure: Novel Validation and Parametric Analysis," *Journal of Building Engineering*, Vol. 44, p. 102533, doi: 10.1016/j.jobe.2021.102533.

Drury, M.M. and Quiel, S.E. (2023a), "Standard versus Natural Fire Resistance for Partially Restrained Composite Floor Beams: 1—Testing," *Journal of Constructional Steel Research*, Vol. 202, p. 107768, doi: 10.1016/j.jcsr.2022.107768.

Drury, M.M. and Quiel, S.E. (2023b), "Standard versus Natural Fire Resistance for Partially Restrained Composite Floor Beams: 2—Analysis," *Journal of Constructional Steel Research*, Vol. 202, p. 107767, doi: 10.1016/j.jcsr.2022.107767.

Franssen, J.-M. and Gernay, T. (2017), "Modeling Structures in Fire with SAFIR®: Theoretical Background and Capabilities," *Journal of Structural Fire Engineering*, Vol. 8, No. 3, pp. 300–323, doi: 10.1108/JSFE-07–2016–0010.

Gamble, W.L. (1989), "Predicting Protected Steel Member Fire Endurance Using Spread-Sheet Programs," *Fire Technology*, Vol. 25, No. 3, pp. 256–273, doi: 10.1007/BF01039782.

Ghojel, J.I. and Wong, M.B. (2005), "Three-Sided Heating of I-Beams in Composite Construction Exposed to Fire," *Journal of Constructional Steel Research*, Vol. 61, No. 6, pp. 834–844, doi: 10.1016/j.jcsr.2004.11.006.

ICC (2020), *IBC: International Building Code, 2021*, International Code Council, Country Club Hills, Ill.

ISO (2019), *Fire Resistance Tests—Elements of Building Construction—Part 11: Specific Requirements for the Assessment of Fire Protection to Structural Steel Elements*, ISO 834–11:2014, International Organization for Standardization, Geneva, Switzerland.

Jiang, S.-C., Ranzi, G., Chen, L.-Z., and Li, G.-Q. (2017), "Behaviour and Design of Composite Beams with Composite Slabs at Elevated Temperatures," *Advances in Structural Engineering*, Vol. 20, No. 10, pp. 1451–1465, doi: 10.1177/1369433216682507.

Khorasani, N.E., Gardoni, P., and Garlock, M. (2015), "Probabilistic Fire Analysis: Material Models and Evaluation of Steel Structural Members," *Journal of Structural Engineering*, Vol. 141, No. 12, p. 04015050, doi: 10.1061/(ASCE)ST.1943–541X.0001285.

Kordosky, A.N., Drury, M.M., and Quiel, S.E. (2020), "Structural Fire Resistance of Partially Restrained, Partially Composite Floor Beams, I: Experiments," *Journal of Constructional Steel Research*, Vol. 167, p. 105945, doi: 10.1016/j.jcsr.2020.105945.

LaMalva, K., Bisby, L., Gales, J., Gernay, T., Hantouche, E., Jones, C., Morovat, A., Solomon, R., and Torero, J. (2020), "Rectification of 'Restrained vs Unrestrained'," *Fire and Materials*, Vol. 44, No. 3, pp. 341–351, doi: 10.1002/fam.2771.

LaMalva, K.J. (Ed.). (2018), *Manual of Practice 138: Structural Fire Engineering*, American Society of Civil Engineers, Reston, Va.

Newman, G. (1999), "The Cardington Fire Tests," *Proceedings of the North American Steel Construction Conference*, AISC, Toronto, Canada, pp. 28.1–28.22.

Ruddy, J., Marlo, J., Ioannides, S., and Alfawakhiri, F. (2003), *Fire Resistance of Structural Steel Framing*, Design Guide 19, AISC, Chicago, Ill.

Selden, K.L. and Varma, A.H. (2016), "Composite Beams under Fire Loading: Numerical Modeling of Behavior," *Journal of Structural Fire Engineering*, Vol. 7, No. 2, pp. 142–157, doi: 10.1108/JSFE-06–2016–011.

UL (2019a), *Fire Resistance Directory*, Underwriters Laboratories Inc., Northbrook, Ill.

UL (2019b), *Fire Resistance Directory: Design No. D982*, Underwriters Laboratories Inc., Northbrook, Ill.

UL (2020), *Standard for Fire Tests of Building Construction and Materials*, UL 263, Underwriters Laboratories, Inc., Northbrook, Ill.

Vinnakota, M.R., Foley, C.M., and Vinnakota, S. (1988), "Design of Partially or Fully Composite Beams with Ribbed Metal Deck Using LRFD Specifications," *Engineering Journal,* AISC, Vol. 25, No. 2, pp. 60–78.

Wang, W., Engelhardt, M.D., Li, G., and Huang, G. (2017), "Behavior of Steel–Concrete Partially Composite Beams Subjected to Fire—Part 1: Experimental Study," *Fire Technology*, Vol. 53, No. 3, pp. 1039–1058, doi: 10.1007/s10694–016–0618-y.

Zhao, B. and Kruppa, J. (1997), *Fire Resistance of Composite Slabs with Profiled Steel Sheet and of Composite Steel Concrete Beams, Part 2: Composite Beams Final Report*, Office for Official Publications of the European Communities, Luxembourg.